

Glass-ceramic joining of Fe22Cr porous alloy to Crofer22APU: interfacial issues and mechanical properties

Fabiana D'Isanto^{1*}, Milena Salvo¹, Sebastian Molin², Damian Koszelow², Hassan
Javed³, Sufyan Akram⁴, Andreas Chrysanthou⁴ and Federico Smeacetto¹.

¹Department of Applied Science and Technology, Politecnico di Torino, Corso Duca degli Abruzzi 24,
10129, Turin, Italy.

²Advanced Materials Centre, Faculty of Electronics, Telecommunications and Informatics, Gdańsk
University of Technology, ul. G. Narutowicza 11/12, 80-233 Gdańsk, Poland.

³Sunfire GmbH, Gasanstaltstraße 2, 01237, Dresden, Germany.

⁴School of Physics, Engineering and Computer Science, University of Hertfordshire, College Lane,
Hatfield, Herts AL10 9AB, UK.

*Corresponding author.

E-mail address: fabiana.disanto@polito.it (F. D'Isanto)

Tel +39 011 0904567

Abstract

This work deals with the joining of porous Fe22Cr ferritic stainless steel to a dense Crofer22APU plate by using a silica-based, Ba-containing glass-ceramic. The chemical and interfacial stability and the mechanical properties of the joints were evaluated before and after thermal ageing at 700°C for 500hrs. The sintering behaviour of the glass was assessed by using heating stage microscopy (HSM) to study the influence of a porous metal substrate on the shrinkage of the joining material. Scanning electron microscopy revealed that there were no defects or cracks at the porous alloy/glass-ceramic interface for both the as-joined samples and the samples after thermal ageing at 700°C for 500 hrs. However, at this exposure temperature, the porous alloy started to form an oxide scale at the interface with the glass-ceramic and the internal surface of

1 the porous alloy. Finally, the evaluation of the mechanical properties by tensile testing
2
3 showed that the properties were not affected by thermal ageing at 700°C.
4
5
6
7

8 **Keywords:** Glass-ceramics; joining; porous alloys; metal-supported SOC
9

10 11 12 13 14 **1. Introduction** 15

16 The porous metallic alloys sector is a major area of interest within the field of high-
17 temperature engineering materials. The functional role of the porosity can be exploited
18 in catalytic reactors (thanks to the high surface area for reactions), filters and metal-
19 supported solid oxide cells (MS-SOCs).
20
21
22
23
24

25 Previous studies have evaluated the oxidation resistance of these alloys in the dense
26 form [1–4] and they have been used for many decades as MS-SOCs [5], but recent
27 studies on high-temperature corrosion of porous metal alloys [6–9] led to increasing
28 interest due to important engineering features such as open porosity which allows gas
29 transport and therefore these materials can be used for gas permeation membranes.
30
31
32
33
34
35
36
37

38 Therefore, porous ferritic stainless steels (FSSs) constitute suitable candidate materials
39 for use as metallic interconnects with high-temperature ceramic fuel cells[9,10] and gas
40 separation membranes [11–13].
41
42
43
44

45 Solid oxide cell (SOC) technology has been developed due to its higher efficiency
46 compared to combustion engines, silent operation and fast charging. Improvements in
47 materials, cell design and manufacturing processing have led to a very high level of
48 technical refinement. More recently, due to the tendency of the cell to fail and
49 assembling issues associated with the use of complex ceramic parts, there has been
50 interest in alternative MS-SOC which can be exploited in the temperature range of 650-
51

1 800°C [14] thanks to their low cost, flexibility, robustness and manufacturability
2
3 benefits. MS-SOCs allow for a lower cost balance of plant components (BoP) and
4
5 higher redox stability.
6

7
8 To choose the most suitable material to produce interconnects, it is desirable to
9
10 match the coefficient of thermal expansion (CTE) of the metal to that of the
11
12 electrolyte[15]. Most manufacturers prefer Fe and Cr-based materials as ferritic
13
14 stainless steels (e.g. 430 alloy), which are commonly used for automotive exhaust
15
16 manifolds and mufflers thanks to their inexpensive and high-temperature resistance.
17
18 This is the reason why FSSs have substituted the more expensive and difficult to
19
20 manufacture ceramic interconnects in SOC design [16,17].
21
22
23

24
25 One of the major challenges in the design of solid oxide cell stacks is the selection
26
27 of joining materials for sealing the metallic interconnect. The sealant role is
28
29 fundamental to assure high durability and long-term performance. The most common
30
31 sealing materials are glass-ceramics due to the simplicity of the sinter-crystallization
32
33 process and the possibility to tailor their composition and thermo-mechanical properties.
34
35 Moreover, several studies have reported that they can exhibit higher gas tightness than
36
37 other typical sealants (i.e. brazing alloys) and superior stability in extreme working
38
39 conditions [18–20]. Another advantage of using glass-ceramics is linked to the presence
40
41 of a residual glassy phase after the sinter-crystallization process, which can minimize
42
43 thermal stresses and provide self-healing properties that are very useful in thermal
44
45 cycling conditions [21]. Furthermore, the formation of crystalline phases within the
46
47 glass phase improves mechanical properties and drives the choice of the composition in
48
49 terms of thermo-mechanical compatibility involving the coefficient of thermal
50
51 expansion (CTE) matching with the SOC components[22].

1 The selected sealant inevitably influences the stability and the chemical
2 compatibility at the interface between the sealant material and the SOC components.
3
4 Some studies have shown that undesirable interfacial reactions are possible between Cr-
5
6 based stainless steels and glass-ceramic sealants. For example, the BaCrO₄ phase that
7
8 has a high CTE (~ 21-23 x 10⁻⁶ K⁻¹) can form at the interface between Ba-containing
9
10 glass-ceramics and Cr-containing metal interconnects [20,23].
11
12
13
14

15 Despite this, many research groups have studied and demonstrated the affinity and
16
17 the effectiveness of glass-based sealants in solid oxide cells [24–27] and many suitable
18
19 BaO-SiO₂-Al₂O₃-based systems have been successfully developed for SOC applications
20
21 [25,28], but the current state of the art associated to the joining of porous to bulk alloys
22
23 in SOCs by glass-based materials is very limited [29].
24
25
26

27 Previous studies [30] carried out oxidation tests of mixed glass-ceramics with FSS
28
29 powders and revealed decreased oxidation rate compared with raw steel powder and
30
31 suggested that the resulting oxide scale can enhance the sealant properties.
32
33
34

35 However, very few studies have dealt with the oxidation processes of porous ferritic
36
37 stainless steels and there has been no detailed investigation of the joining and
38
39 integration issues of these materials. A systematic understanding of how the stainless-
40
41 steel porosity and the consequent corrosion reactions affect the interfacial behaviour
42
43 with glass-based materials is still lacking.
44
45
46

47 This study describes the joining of porous Fe22Cr alloy to a dense Crofer 22APU
48
49 plate with a silica barium-based glass-ceramic. The interfacial behaviour between the
50
51 silica barium-based glass-ceramic and both dense and porous alloy interconnects will be
discussed with particular focus on the morphological and chemical characterisation at
the interface before and after thermal ageing at 700°C for 500 h in air. Finally, tensile

1 tests were performed on joined samples, comparing the tensile strength and the fracture
2 surface between as-joined and aged specimens.
3
4
5
6
7

8 **2. Materials and methods**

9

10
11 The Fe22Cr porous alloy substrate (of composition Cr = 22 wt.%; Mn = 0.23 wt.%; Si =
12 0.08 wt.%; Ni, Cu, Mo <0.03 wt.%, with Fe representing the balance), was produced by
13
14 Höganas AB (Höganas, Sweden) and characterised for its resistance against high
15
16 temperature oxidation in a study by Koszelow et al [9]. The ~0.4 mm thick porous sheet
17
18 was manufactured by tape-casting of a steel particle slurry, followed by drying,
19
20 debinding and sintering at 1250°C in a pure H₂ atmosphere for 30 minutes. Dense steel
21
22 coupons were cut from a 0.3-mm-thick plate of Crofer22APU (Cr = 23 wt.%, Mn = 0.45
23
24 wt.%, La = 0.1 wt.%, Ti = 0.06 wt.%, Si and Al < 0.05 wt.% with Fe representing the
25
26 balance) provided by VDM Metals (Verdohl, Germany). Both porous and dense
27
28 substrates were cleaned in acetone and ethanol for 10 min each in an ultrasonic bath.
29
30
31 The joining material was a Ba-based glass-ceramic, referred to as GC2 [31]. The
32
33 original glass was produced using conventional melting and casting from the following
34
35 high-purity grade raw materials: SiO₂ (Sigma Aldrich, 99.5 % purity) with 55 mol%,
36
37 B₂O₃(precursor H₃BO₃, Sigma Aldrich, 99% purity) with 8 mol%, Al₂O₃ (Alfa Aesar,
38
39 99.9 % purity) with 4 mol%, CaO (precursor CaCO₃ Sigma Aldrich, 99 % purity) with 7
40
41 mol % and BaO (precursor Ba₂CO₃ Thermoscientific, 99.8 % purity) with 26 mol%. All
42
43 the raw material powders were mixed for 24 hrs and melted in a Pt-Rh crucible in an
44
45 electric furnace (LHT418PN2, Nabertherm GmbH, Lilienthal/ Bremen, Germany) in air
46
47 at 1500 °C for 1 h (the first 30 minutes a lid covered the crucible). The melt was cast
48
49 onto a metal plate and the glass was subsequently ball-milled and sieved (particle
50
51

1 size < 38 μm). The sintering behaviour of the glass powders on the porous substrate, as
2
3 well as on Al_2O_3 inert substrate was investigated using heating stage microscopy (HSM;
4 Hesse Heating Microscope, Germany), with a heating rate of $5^\circ\text{C}/\text{min}$, from room
5
6 temperature up to the melting point identified by the instrument.
7
8

9
10 A small quantity of a slurry paste composed of ethanol (70 wt.%) and glass powder (30
11 wt.%) was manually deposited with a spatula between the two metal alloys (squared
12 specimens $\sim 11\text{ mm} \times \sim 11\text{ mm}$) to be joined. Preliminary tests carried out with different
13 configurations led to the most effective joint with pre-oxidised (900°C , 2h as dwelling
14 time, at a $5^\circ\text{C}/\text{min}$ as heating/cooling rate) dense Crofer22APU placed on the top. The
15 joining process was carried out in air at 950°C for 1h ($5^\circ\text{C}/\text{min}$ as heating/cooling rate)
16 in a muffle furnace (L5/13/P330, Nabertherm GmbH, Lilienthal/ Bremen, Germany).
17

18 During the heat treatment, a stainless-steel weight was placed on top of the sandwich
19 structure to apply a pressure of around 1.5 kPa. A Computed Tomography (CT) scan
20 (Fraunhofer IKTS, Hermsdorf, Germany) was used to obtain morphological and
21 qualitative density information of the joined sample under the following parameters:
22
23 9.25 μm as resolution, 280kV as acceleration voltage and 1s the exposure time for each
24 projection. The reconstruction of the joint consists of creating a 3D model of the
25 analysed volume by the CT software.
26
27

28 The same heat treatment identified for the joined sample was also used to produce a dry
29 pressed glass-ceramic pellet, using uniaxial pressure of 12 MPa, to thermo-
30 mechanically characterise GC2 glass-ceramic. The coefficient of thermal expansion
31 (CTE) and the dilatometric softening point of as-cast GC2 glass and as-joined glass-
32 ceramic were measured using a dilatometer (Netzsch, DIL 402 PC) equipped with an
33
34
35
36
37
38
39
40
41
42
43
44
45
46
47
48
49
50
51

1 alumina sample holder, at a heating rate of 5°C/min, applying a constant compressive
2
3 force, between the sample and the piston of 0.25N.
4

5
6 Some joined samples were cross-sectioned and prepared for SEM and EDS analyses,
7
8 while others were subjected to ageing treatment at 700°C for 500 hrs in a muffle furnace
9
10 (Carbolite Gero, Hope Valley, UK). This temperature was chosen based on the results
11
12 obtained by Koszelow et al. [9] focused on the corrosion study of the same Fe22Cr
13
14 porous alloy up to 900°C. Some joint samples underwent tensile testing before and after
15
16 thermal ageing using a method modified from the ASTM C633-01 standard. The tests
17
18 were carried out using a Syntech 10/D machine (MTS Systems Corporation, Minnesota,
19
20 USA). Each joint was adhered to two loading fixtures (Figure 1) by using Araldite®
21
22 2015 epoxy resin and thermally treated at 85°C for 1h to crosslink. The cross-head
23
24 speed was set to 0.5 mm/min. The tensile strength was calculated by dividing the
25
26 maximum force by the area of the joint which measured 11 mm x 11 mm. A field-
27
28 emission scanning electron microscope (FESEM; SupraTM 40, Zeiss, Oberkochen,
29
30 Germany) equipped with an energy dispersive X-ray analyser (EDS, Bruker, Germany)
31
32 was used to characterise the morphology of the samples, which were previously
33
34 polished using SiC papers (grit size 600-4000) and coated with Cr. A benchtop scanning
35
36 electron microscope (SEM, JCM-6000 plus, Jeol, Peabody, Massachusetts, USA) was
37
38 used to observe the fractured surface of the samples following mechanical testing. X-
39
40 ray diffraction (XRD) analysis of the fractured surface of a joined sample after ageing
41
42 was conducted using an X'Pert Pro MRD diffractometer, with Cu K α radiation
43
44 (PANalytical X'Pert Pro, Philips, Almelo, The Netherlands), and with the aid of X-Pert
45
46 HighScore software, while the phases were identified using the JCPDS database
47
48
49
50
51

1 provided by PDF-4 ICDD (International Centre for Diffraction Data, Newton Square,
2
3 Pennsylvania, the USA).
4

5
6 **Figure 1.** Configuration used for the mechanical tensile test.
7

8 9 **3. Results and Discussion**

10
11 **Figure 2** reports the experimental curves obtained from heating stage microscopy
12 (HSM) analyses of the as-cast GC2 glass powder pellets on the porous Fe22Cr alloy
13 (curve 1) and on an inert Al₂O₃ support (curve 2), where the linear shrinkages % are
14 (curve 1) and on an inert Al₂O₃ support (curve 2), where the linear shrinkages % are
15 plotted against the temperature. The first two characteristic temperatures are the points
16 at which linear shrinkage of the glass starts (T_{fs}) and assumes the maximum value (T_{ms}):
17 they are 705°C and 790°C on the porous alloy, 696°C and 802°C on the Al₂O₃
18 substrate. The temperature at which the first signs of softening are observed (DT) was
19 identified at 811°C (onto Fe22Cr) and 822°C (onto Al₂O₃), while the sphere
20 temperature (ST) was at 893°C on the porous alloy and 872°C on Al₂O₃, where the
21 height of the sample is equal to the width of the base. The half-sphere temperature (HT),
22 which is the temperature at which the height of the sample is half the width of the base,
23 was measured at 1028°C on the Fe22Cr porous alloy and at 1040°C on the inert
24 substrate. Finally, the flow temperature (FT) was evident at 1079°C and 1076°C; the
25 latter is the temperature at which the height of the sample drops to below one-third of
26 the base. A visible plateau between 800 and 1000°C was observed and this represents
27 the crystallization phenomenon that occurs. A significant expansion of the glass
28 powder pellet is visible for the GC2 glass onto the Fe22Cr porous alloy, which is
29 evidently absent on the inert substrate; this is likely due to gaseous species developed at
30 T higher than 920°C, determined by the oxidation of the porous alloy during the GC2
31 viscous flow sintering. Based on these observations, the conditions for joining the
32
33
34
35
36
37
38
39
40
41
42
43
44
45
46
47
48
49
50
51

1 porous samples to the bulk alloys were determined to be a temperature of 950°C with a
2
3 dwelling time of 1h in air. This sinter-crystallization heat treatment led to the formation
4
5 of GC2 glass-ceramic with BaSi₂O₅ as crystalline phase (CTE ~ 12.5 x 10⁻⁶ K⁻¹),
6
7 obtained by the partial devitrification of the GC2 parent glass [32].
8
9

10
11 **Figure 2.** Heating Stage Microscopy (HSM) curves of the GC2 glass (5°C/min heating rate) on the
12 Fe22Cr porous alloy (curve 1) and on the inert Al₂O₃ support (curve 2); characteristic temperatures
13
14 of GC2 glass identified with HSM are shown below the figure.
15
16
17

18
19 In order to evaluate the thermo-mechanical properties of the microstructure obtained
20
21 with the above-mentioned joining thermal treatment, dilatometry was used to measure
22
23 the coefficient of thermal expansion (CTE) of the GC2 glass-ceramic as well as that of
24
25 the parent glass (**Figure 3**). The CTE value of the GC2 as-cast glass is 9.2 x 10⁻⁶ K⁻¹
26
27 between 200-500°C, while the glass transition temperature (T_g) and the dilatometric
28
29 softening point are 665°C and 688°C respectively (**Figure 3**, curve 1). It can be
30
31 observed from the dilatometric analysis of the GC2 glass-ceramic that T_g is slightly
32
33 lower (658°C) with respect to the original glass and within experimental error, while the
34
35 softening point is the same. However, there was evidence of an increase in the
36
37 coefficient of thermal expansion of the glass-ceramic (10.7 x 10⁻⁶ K⁻¹) in comparison
38
39 with that of the GC2 glass as suggested by the change in the slope of the curve (**Figure**
40
41 **3**, curve 2). The transformation of the parent glass into a glass ceramic led to a
42
43 significant improvement of the CTE in the view of the thermomechanical compatibility
44
45 of the final joined structure, since the CTEs of both the substrates to be joined
46
47 (Crofer22APU and Fe22Cr) are around 11 x 10⁻⁶ K⁻¹ (200-700°C).
48
49
50
51

52
53 **Figure 3.** Dilatometric curves of the GC2 as-cast glass (curve 1) and GC2 glass-ceramic obtained
54 after sinter-crystallization at 950°C for 1h (curve 2); 5°C/min heating rate.

1
2
3 The sandwiched samples were processed, using the procedure described in the
4
5 experimental section.
6

7
8 As observed in [Figure 4 a](#), the SEM image of the cross-section of the joined sample
9
10 showed excellent adhesion of the GC2 glass-ceramic with both the porous and dense
11
12 metal alloys. No cracks or delamination are visible at the glass-ceramic/substrates
13
14 interface resulting in a continuous joint along the entire length of the interface.
15
16 Furthermore, there was no evidence of any reactions taking place by the interaction
17
18 between the Crofer22APU/porous alloy and the glass ([Figure 4 b,c](#)) ; an average joint
19
20 thickness of 520 μm was obtained using a pressure of 1.5 kPa. The presence of a few
21
22 closed pores, homogeneously distributed in the glass-ceramic, could probably be due to
23
24 the manual slurry method used to produce the joined specimens. On the other side, the
25
26 larger voids observed only at the Fe22Cr porous alloy/GC2 glass-ceramic interface is
27
28 probably due to gaseous species released from the porous substrate during sintering
29
30 which occurred by viscous flow. Further SEM investigation carried out on a
31
32 Crofer22APU/GC2 glass-ceramic/Crofer22APU joint (not reported here), showed the
33
34 absence of these such big voids at both dense alloy/glass-ceramic interfaces, thus
35
36 confirming that the bigger porosity is due only to the presence of the Fe22Cr porous
37
38 alloy.
39

40
41
42 [Figure 4](#). SEM images of the cross-section of (a) Crofer22APU/GC2 glass-ceramic/Fe22Cr porous
43
44 alloy, (b) Crofer22APU/GC2 glass-ceramic interface (back-scattered) and (c) GC2 glass-
45
46 ceramic/Fe22Cr porous alloy interface (back-scattered) obtained after sinter-crystallization at 950°C
47
48 for 1h.
49
50
51

1 Most of the porosity was concentrated at the porous alloy/GC2 glass-ceramic interface
2
3 as evidenced by SEM as well as computed tomography (CT) that was carried out on a
4
5 joined sandwich-like specimen (Figure 5). In Figure 5a, a reconstructed 3D model of
6
7 the sample is shown, while in the other images (Figure 5 b-d), 3 cross-sections are
8
9 represented at a different distance from the porous alloy surface; these scans were taken
10
11 close to the Fe22Cr/GC2 glass-ceramic interface (Figure 5b), in the middle of the
12
13 joining area (Figure 5c) and finally further from the interface with the porous alloy. It is
14
15 evident that most voids are located at the Fe22Cr/GC2 glass-ceramic interface, while in
16
17 the other sections very few pores are shown.
18
19
20
21
22

23 **Figure 5.** CT-scan of a Crofer22APU/GC2 glass-ceramic/Fe22Cr porous alloy joined sample
24 thermally treated at 950°C for 1 h. (a) 3D-model; sectioning plane (b) close to the porous alloy, (c)
25 in the middle of the glass-ceramic, (d) close to Crofer22APU. The big pore on the right could be due
26 to the manual slurry method used to produce the joined specimen.
27
28
29
30
31

32
33 More details concerning the Fe22Cr porous alloy/GC2 glass-ceramic interface are
34 shown in FE-SEM images on a cross-sectioned joined sample in Figure 6. Close
35 inspection at the interface shows that, despite the presence of pores that are concentrated
36 in the lower part of the joining area, no cracks are located both in the joining area and at
37 the interface. Strong adhesion between the GC2 glass-ceramic and the porous substrate
38 can be observed (Figure 6a). The distribution of the crystalline phases produces a dense
39 network of needle-like interlocked crystallites embedded in the residual glassy phase.
40 EDS analysis in Figure 6d (spectrum 1) revealed the presence of Ba, Si and O,
41 indicating the crystallization of a BaSi₂O₅ crystalline phase, homogeneously dispersed
42 within the darker glassy matrix which reasonably shows a higher level of Al and Ca and
43 a lower content of Ba and Si (spectrum 2); this hypothesis was supported by XRD
44
45
46
47
48
49
50
51

1 diffraction pattern of GC2 glass-ceramic after joining heat treatment at 950°C, 1h in air,
2
3 as reported by Smeacetto et al. [32]. As shown in Figure 6c and the corresponding EDS
4
5 in Figure 6d (spectrum 3), the glass infiltrates the porous alloy very well during the
6
7 sinter-crystallization treatment; infiltration distance levels of up to 50 μm from the GC2
8
9 glass-ceramic/Fe22Cr porous alloy interface are evident.
10
11
12

13
14 **Figure 6.** Cross-section FE-SEM images at lower (a) and higher (b) magnification of the Fe22Cr
15 porous alloy/GC2 glass-ceramic interface after sinter-crystallization at 950°C for 1h; (c) infiltration
16 of the glass-ceramic in the porous alloy of the joined sample; (d) EDS analyses of the GC2 glass-
17 ceramic in the joining area.
18
19
20
21
22

23 Tensile testing was used to evaluate the mechanical properties of the joined
24 samples. The tests carried out on as-joined Crofer22APU/GC2 glass-ceramic/Fe22Cr
25 porous alloy samples showed an average tensile strength of 7.4 ± 0.5 MPa (identified
26 with σ_m in Figure 7). This value is slightly higher than the tensile strength of the
27 majority of glass-ceramic sealants reported in the literature (3.8-6.3 MPa) and used for
28 joining Crofer22APU and Crofer22H [33].
29
30
31
32
33
34
35
36
37

38
39 **Figure 7.** Macrographs of as-joined and aged Crofer22APU/GC2glass-ceramic/ Fe22Cr samples
40 after tensile testing.
41
42

43 Macrographs of the fracture surface of 3 as-joined specimens are shown in Figure 7.
44 While most of the fractured area of the Fe22Cr porous substrate in Figure 7 seems to
45 show exposed metal alloy, however, EDS analyses (not reported here) revealed many
46 parts of the surface covered by the GC2 glass-ceramic; in some areas, large sections (in
47 white) of the GC2 glass-ceramic suggest the presence of cohesive failure, while small
48 white specks show evidence of fractured glass-ceramic that had impregnated the pores
49 of the Fe22Cr substrate. Inspection of the opposite part shows small fractured black
50
51

1 specks of Fe22Cr embedded in the GC2 glass-ceramic. These observations suggest that
2
3 the impregnation of the glass-ceramic into the Fe22Cr porous alloy enhances the
4
5 interfacial strength. Indeed, part of the failure seems to be occurring in the porous
6
7 Fe22Cr just beyond the area of GC2 impregnation due to stress concentration in the
8
9 porous alloy (due to the absence of GC2 glass-ceramic). Overall there is mixed
10
11 adhesive/cohesive failure, where the adhesive failure is mainly localised at the
12
13 porous/GC2 interface. [Figure 8a](#) shows a magnified fracture surface of the glass-
14
15 ceramic on the Crofer22APU side after mechanical testing; the bright phase well visible
16
17 in the back-scattered SEM image identified by the EDS analysis as BaCrO₄, was mainly
18
19 located on the edges of the joined area and was present on both the porous and the dense
20
21 metal alloy.
22
23
24
25
26

27
28 [Figure 8](#). SEM images of top views of fracture surface of an as-joined (a) and an aged (b)
29
30 Crofer22APU/GC2glass-ceramic/ Fe22Cr porous alloy sample after mechanical testing
31
32 (Crofer22APU side); EDS analyses carried out on the fracture surfaces in the joining area.
33
34
35

36
37 [Figure 9](#) shows a cross-section of a joined sample after ageing at 700°C for 500 hrs.
38
39 There was no evidence of cracks following ageing, thus implying that detrimental
40
41 thermal stresses did not occur. In addition, the microstructure of the GC2 glass-ceramic
42
43 did not seem to be affected by the heat treatment ([Figure 9a](#)). However, [Figure 9b](#)
44
45 shows evidence of the formation of an oxidation scale on the pores surface; oxidation
46
47 was also apparent at the GC2 glass-ceramic/porous alloy interface ([Figure 9c](#)). Due to
48
49 the large surface/volume ratio of the porous samples, there is a risk that oxide formation
50
51 (typically Cr₂O₃ [34]) can potentially lead to depletion of Cr within the porous alloy. In
a previously cited work [9], the surface of the same porous alloy, which was exposed to
a temperature of 700°C for 100hrs, did not show any significant microstructural changes

1 in comparison to alloy samples that had not been aged. The weight gain at 700°C after
2
3
4 100 hrs was reported to be around 1%. However, a sample that had been exposed to
5
6 750°C for the same time, experienced a weight gain of ~2.5 % and was characterised by
7
8 changes at the surface; a small amount of oxide had clearly formed at the surface which
9
10 exhibited signs of greater roughness which may have resulted by the fact that the
11
12 surface of the porous alloy was slightly rough. From [Figure 9d](#) the formation of a
13
14 darker layer covering the Fe22Cr porous alloy following ageing is apparent. Based on
15
16 the results of the EDS analysis the scale seems to be composed of a mixed Fe and Cr-
17
18 based oxide and, since the latter is visible also further from the glass-ceramic/Fe22Cr
19
20 porous alloy interface, it could be due to a longer ageing heat treatment (700°C for
21
22 500hrs).

23
24
25
26
27 [Figure 9](#). FE-SEM images of a cross-section after ageing at 700°C for 500hrs: (a,c) Fe22Cr porous
28
29 alloy/GC2 glass-ceramic interface and (b) Fe22Cr porous alloy; (d) higher magnification of Fe22Cr
30
31 porous alloy and EDS analysis carried out on the porosity edge of the porous alloy.
32
33

34
35
36 The results of mechanical testing for the thermally-aged samples exhibited an
37
38 average tensile strength of 7.7 ± 2.9 MPa, a value that was similar to the as-joined
39
40 samples. Inspection of the macrographs in [Figure 7](#) shows that the samples suffered a
41
42 completely or mainly adhesive failure. [Figure 8b](#) shows a higher magnification of the
43
44 fracture surface of the Crofer22APU after ageing at 700°C for 500 hrs following
45
46 mechanical testing. The EDS analysis showed high atomic% of Ba and Cr and therefore
47
48 the presence of barium chromate can be hypothesized also after ageing .
49
50
51

XRD analysis that was carried out on the Crofer22APU side (on the porous side, the remaining glass-ceramic layer was not enough) after ageing and mechanical testing, is shown in [Figure 10](#). The main peaks matched with those of the orthorhombic barium

1 silicate (Sanbornite with chemical formula BaSi_2O_5 , PDF card n. 01-071-1441), which
2
3 was the main phase present after ageing. Prior to the ageing treatment, the only phase
4
5 that was present was BaSi_2O_5 as previously reported for the as joined glass-ceramic
6
7 system before ageing heat treatment [32]. However, following ageing, new phases
8
9 emerged like those reported in previous studies with similar glasses [25], where the
10
11 formation of additional Ba-Ca-silicate phases that were not homogeneously distributed
12
13 within the microstructure was observed. In the present work a secondary phase
14
15 identified as the barium calcium boron silicate (named Itsiite[35], crystal system:
16
17 tetragonal; space group: I-42m) $\text{Ba}_2\text{CaSi}_4\text{B}_2\text{O}_{14}$, with PDF card n. 04-021-1159 was
18
19 found. In addition, some low-intensity peaks were identified as the BaCrO_4 phase,
20
21 confirming the EDS analyses carried out at the same fracture surface. Finally, the three
22
23 peaks at about $2\theta=22.8^\circ$, $2\theta = 30.2^\circ$ and $2\theta=34.5^\circ$ could likely be attributed to
24
25 $\text{BaAl}_2\text{Si}_2\text{O}_8$ (ref. code 00-012-0725). In the present work, the glass-ceramic joining
26
27 material was subjected to a thermal ageing temperature that was 40°C higher than the
28
29 GC2 glass-ceramic T_g value. These findings, while preliminary, suggest that this
30
31 system is prone to further devitrification at temperatures slightly above the T_g . Despite
32
33 this, the mechanical behaviour of the joints is not affected by this microstructural
34
35 rearrangement. Further research should be undertaken to investigate the
36
37 thermomechanical behaviour at temperatures higher than 700°C .
38
39
40
41
42
43
44
45
46
47
48
49
50
51

Figure 10. XRD pattern of the fracture surface (Crofer22APU side) of a Fe22Cr/GC2 glass-ceramic/Crofer22APU joined sample after ageing at 700°C for 500 hrs.

4. Conclusions

1 The possibility of using porous metal alloys provides interesting engineering
2
3 features thanks to their functional porosity, which make these candidate materials for
4
5 metal-supported solid oxide cells. The development of a dense to a porous joint can
6
7 play a key role in the manufacture of reliable, efficient and durable metal-supported
8
9 SOCs. The novelty of this study concerns the joining of porous stainless steel to a
10
11 dense one with a glass-ceramic obtained from sinter-crystallization of a glass sealant.
12
13 Different aspects concerning the interfacial issues and mechanical properties were
14
15 discussed, evaluating an optimal adhesion and mechanical stability in
16
17 Crofer22APU/GC2 glass-ceramic/ Fe22Cr porous alloy joints, before and after thermal
18
19 ageing carried out at 700°C for 500hrs. The morphological analysis found no defects or
20
21 cracks at the porous alloy/glass-ceramic interface, neither in the as-joined samples nor
22
23 in samples after ageing at 700°C for 500 hrs. However, at this temperature, the porous
24
25 alloy started to experience the formation of an oxidation scale at the interface between
26
27 the Fe22Cr porous alloy and the GC2 glass-ceramic, as well as around the wall of the
28
29 pores of the porous alloy. The mechanical strength of the joined samples was not
30
31 affected by thermal ageing (7.4 MPa±0.5 before and 7.7 MPa ±2.9 after ageing).
32
33
34
35
36
37
38

39 The current study provides the first assessment concerning the joining of a porous
40
41 to a dense alloy using glass-ceramics and makes the groundwork for future research into
42
43 MS-SOC development.
44
45
46
47
48
49

50 **Acknowledgments**

51 DK and SM acknowledge the support of National Science Centre Poland (NCN)
Sonata Bis 8 project number 2018/30/E/ST8/00821 “High-temperature corrosion studies

1 and development of oxidation lifetime model of alloy powders and sintered porous alloys:
2
3 effects of composition and microstructure”.

9 **Declaration of competing interest**

10
11 The authors declare that they have no known competing financial interests or personal
12
13 relationships that could have appeared to influence the work reported in this paper.
14
15

18 **References**

- 20
21 [1] J.E. Hammer, S.J. Laney, R.W. Jackson, K. Coyne, F.S. Pettit, G.H. Meier, The
22
23 oxidation of ferritic stainless steels in simulated solid-oxide fuel-cell atmospheres,
24
25 Oxid. Met. 67 (2007) 1–38. <https://doi.org/10.1007/s11085-006-9041-y>.
26
27
28 [2] N.J. Magdefrau, L. Chen, E.Y. Sun, M. Aindow, Effects of alloy heat treatment on
29
30 oxidation kinetics and scale morphology for crofer 22 APU, J. Power Sources. 241
31
32 (2013) 756–767. <https://doi.org/10.1016/j.jpowsour.2013.03.181>.
33
34
35 [3] P. Alnegren, M. Sattari, J. Froitzheim, J.E. Svensson, Degradation of ferritic
36
37 stainless steels under conditions used for solid oxide fuel cells and electrolyzers at
38
39 varying oxygen pressures, Corros. Sci. 110 (2016) 200–212.
40
41 <https://doi.org/10.1016/j.corsci.2016.04.030>.
42
43
44 [4] B. Timurkutluk, S. Toros, S. Onbilgin, H.G. Korkmaz, Determination of
45
46 formability characteristics of Crofer 22 APU sheets as interconnector for solid
47
48 oxide fuel cells, Int. J. Hydrogen Energy. 43 (2018) 14638–14647.
49
50 <https://doi.org/10.1016/j.ijhydene.2018.04.243>.
51
52 [5] S. Fontana, R. Amendola, S. Chevalier, P. Piccardo, G. Caboche, M. Viviani, R.
Molins, M. Sennour, Metallic interconnects for SOFC: Characterisation of

- 1 corrosion resistance and conductivity evaluation at operating temperature of
2 differently coated alloys, *J. Power Sources*. 171 (2007) 652–662.
3
4
5
6 <https://doi.org/10.1016/j.jpowsour.2007.06.255>.
7
- [6] D.N. Boccaccini, H.L. Frandsen, B.R. Sudireddy, P. Blennow, H. Persson, K.
8 Kwok, P. Vang Hendriksen, Creep behaviour of porous metal supports for solid
9 oxide fuel cells, *Int. J. Hydrogen Energy*. 39 (2014) 21569–21580.
10
11 <https://doi.org/10.1016/j.ijhydene.2014.07.138>.
12
13
- [7] M. Stange, C. Denonville, Y. Larring, A. Brevet, A. Montani, O. Sicardy, J.
14 Mougín, P.O. Larsson, Improvement of corrosion properties of porous alloy
15 supports for solid oxide fuel cells, *Int. J. Hydrogen Energy*. 42 (2017) 12485–
16 12495. <https://doi.org/10.1016/j.ijhydene.2017.03.170>.
17
18
- [8] E. Stefan, C. Denonville, Y. Larring, M. Stange, R. Haugrud, Oxidation study of
19 porous metal substrates for metal supported proton ceramic electrolyzer cells,
20 *Corros. Sci.* 164 (2020) 108335. <https://doi.org/10.1016/j.corsci.2019.108335>.
21
22
23
24
- [9] D. Koszelow, M. Makowska, F. Marone, J. Karczewski, P. Jasiński, S. Molin, High
25 temperature corrosion evaluation and lifetime prediction of porous Fe22Cr
26 stainless steel in air in temperature range 700–900 °C, *Corros. Sci.* 189 (2021).
27 <https://doi.org/10.1016/j.corsci.2021.109589>.
28
29
30
31
32
33
- [10] V. Venkatachalam, S. Molin, M. Chen, I. Smirnov, P.O. Larsson, P. V.
34 Hendriksen, N. Bonanos, Optimization of ferritic steel porous supports for protonic
35 fuel cells working at 600°C, *Mater. Sci. Technol. Conf. Exhib. 2014, MS T 2014*.
36 2 (2014) 1231–1239.
37
38
- [11] Y. Xing, S. Baumann, D. Sebold, M. Rüttinger, A. Venskutonis, W.A.
39 Meulenberg, D. Stöver, Chemical compatibility investigation of thin-film oxygen
40
41
42
43
44
45
46
47
48
49
50
51

- 1 transport membranes on metallic substrates, *J. Am. Ceram. Soc.* 94 (2011) 861–
2 866. <https://doi.org/10.1111/j.1551-2916.2010.04171.x>.
- 3
4
5
6 [12] J.A. Calles, R. Sanz, D. Alique, Influence of the type of siliceous material used as
7 intermediate layer in the preparation of hydrogen selective palladium composite
8 membranes over a porous stainless steel support, *Int. J. Hydrogen Energy.* 37
9 (2012) 6030–6042. <https://doi.org/10.1016/j.ijhydene.2011.12.164>.
- 10
11
12
13 [13] J.A. Glasscock, L. Mikkelsen, Å.H. Persson, G. Pećanac, J. Malzbender, P.
14 Blennow, F. Bozza, P. V. Hendriksen, Porous Fe₂₁Cr₇Al₁Mo_{0.5}Y metal supports
15 for oxygen transport membranes: Thermo-mechanical properties, sintering and
16 corrosion behaviour, *Solid State Ionics.* 242 (2013) 33–44.
17 <https://doi.org/10.1016/j.ssi.2013.04.006>.
- 18
19
20
21 [14] S. Linderoth, Solid oxide cell R&D at Risø National Laboratory-and its transfer to
22 technology, *J. Electroceramics.* 22 (2009) 61–66. [https://doi.org/10.1007/s10832-](https://doi.org/10.1007/s10832-008-9458-6)
23 [008-9458-6](https://doi.org/10.1007/s10832-008-9458-6).
- 24
25
26
27 [15] M.C. Tucker, Progress in metal-supported solid oxide fuel cells: A review, *J.*
28 *Power Sources.* 195 (2010) 4570–4582.
29 <https://doi.org/10.1016/j.jpowsour.2010.02.035>.
- 30
31
32
33 [16] M.C. Tucker, G.Y. Lau, C.P. Jacobson, L.C. DeJonghe, S.J. Visco, Stability and
34 robustness of metal-supported SOFCs, *J. Power Sources.* 175 (2008) 447–451.
35 <https://doi.org/10.1016/j.jpowsour.2007.09.032>.
- 36
37
38
39 [17] M.C. Tucker, Durability of symmetric-structured metal-supported solid oxide fuel
40 cells, *J. Power Sources.* 369 (2017) 6–12.
41 <https://doi.org/10.1016/j.jpowsour.2017.09.075>.
- 42
43
44
45 [18] J.W. Fergus, Sealants for solid oxide fuel cells, *J. Power Sources.* 147 (2005) 46–
46
47
48
49
50
51

- 1 57. <https://doi.org/10.1016/j.jpowsour.2005.05.002>.
- 2
- 3 [19] M.K. Mahapatra, K. Lu, Seal glass for solid oxide fuel cells, *J. Power Sources*. 195
- 4 (2010) 7129–7139. <https://doi.org/10.1016/j.jpowsour.2010.06.003>.
- 5
- 6 [20] N. Mahato, A. Banerjee, A. Gupta, S. Omar, K. Balani, Progress in material
- 7 selection for solid oxide fuel cell technology: A review, *Prog. Mater. Sci.* 72 (2015)
- 8 141–337. <https://doi.org/10.1016/j.pmatsci.2015.01.001>.
- 9
- 10 [21] R.N. Singh, Sealing Technology for Solid Oxide Fuel Cells (SOFC), *Int. J. Appl.*
- 11 *Ceram. Technol.* 4 (2007) 134–144. [https://doi.org/10.1111/j.1744-](https://doi.org/10.1111/j.1744-7402.2007.02128.x)
- 12 7402.2007.02128.x.
- 13
- 14 [22] F. Smeacetto, A. De Miranda, A. Chrysanthou, E. Bernardo, M. Secco, M. Bindi,
- 15 M. Salvo, A.G. Sabato, M. Ferraris, Novel glass-ceramic composition as sealant
- 16 for SOFCs, *J. Am. Ceram. Soc.* 97 (2014) 3835–3842.
- 17 <https://doi.org/10.1111/jace.13219>.
- 18
- 19 [23] M.K. Mahapatra, K. Lu, Glass-based seals for solid oxide fuel and electrolyzer
- 20 cells - A review, *Mater. Sci. Eng. R Reports*. 67 (2010) 65–85.
- 21 <https://doi.org/10.1016/j.mser.2009.12.002>.
- 22
- 23 [24] S.M. Gross, T. Koppitz, J. Rimmel, J.B. Bouche, U. Reisgen, Joining properties
- 24 of a composite glass-ceramic sealant, *Fuel Cells Bull.* 2006 (2006) 12–15.
- 25 [https://doi.org/10.1016/S1464-2859\(06\)71320-7](https://doi.org/10.1016/S1464-2859(06)71320-7).
- 26
- 27 [25] J. Schilm, A. Rost, M. Kusnezoff, S. Megel, A. Michaelis, Glass ceramics sealants
- 28 for SOFC interconnects based on a high chromium sinter alloy, *Int. J. Appl. Ceram.*
- 29 *Technol.* 15 (2018) 239–254. <https://doi.org/10.1111/ijac.12811>.
- 30
- 31 [26] H. Javed, A.G. Sabato, K. Herbrig, D. Ferrero, C. Walter, M. Salvo, F. Smeacetto,
- 32 Design and characterization of novel glass-ceramic sealants for solid oxide
- 33
- 34
- 35
- 36
- 37
- 38
- 39
- 40
- 41
- 42
- 43
- 44
- 45
- 46
- 47
- 48
- 49
- 50
- 51

- 1 electrolysis cell (SOEC) applications, *Int. J. Appl. Ceram. Technol.* 15 (2018) 999–
2
3
4 1010. <https://doi.org/10.1111/ijac.12889>.
- 5
6 [27] A.G. Sabato, A. Chrysanthou, M. Salvo, G. Cempura, F. Smeacetto, Interface
7
8 stability between bare, Mn–Co spinel coated AISI 441 stainless steel and a
9
10 diopside-based glass-ceramic sealant, *Int. J. Hydrogen Energy.* 43 (2018) 1824–
11
12 1834. <https://doi.org/10.1016/j.ijhydene.2017.11.150>.
- 13
14
15 [28] J. Schilm, A. Rost, M. Kusnezoff, A. Michaelis, Sealing Glasses for SOFC -
16
17 Degradation Behaviour, in: *Adv. Solid Oxide Fuel Cells V*, 2010: pp. 183–193.
18
19 <https://doi.org/10.1002/9780470584316.ch17>.
- 20
21
22 [29] D. Udomsilp, J. Rechberger, R. Neubauer, C. Bischof, F. Thaler, W. Schafbauer,
23
24 N.H. Menzler, L.G.J. de Haart, A. Nenning, A.K. Opitz, O. Guillon, M. Bram,
25
26 Metal-Supported Solid Oxide Fuel Cells with Exceptionally High Power Density
27
28 for Range Extender Systems, *Cell Reports Phys. Sci.* 1 (2020).
29
30 <https://doi.org/10.1016/j.xcrp.2020.100072>.
- 31
32
33 [30] A. Drewniak, D. Koszelow, P. Błaszczak, K. Górnicka, K. Jurak, H. Javed, A.G.
34
35 Sabato, P. Jasiński, S. Molin, F. Smeacetto, Glass-ceramic sealants and steel
36
37 interconnects: Accelerated interfacial stability and reactivity tests at high
38
39 temperature, *Mater. Des.* 212 (2021).
40
41 <https://doi.org/10.1016/j.matdes.2021.110259>.
- 42
43
44 [31] M. Ferraris, S. De la Pierre, A.G. Sabato, F. Smeacetto, H. Javed, C. Walter, J.
45
46 Malzbender, Torsional shear strength behavior of advanced glass-ceramic sealants
47
48 for SOFC/SOEC applications, *J. Eur. Ceram. Soc.* 40 (2020) 4067–4075.
49
50 <https://doi.org/10.1016/j.jeurceramsoc.2020.04.034>.
- 51
[32] F. Smeacetto, A. Chrysanthou, A.G. Sabato, H. Javed, S.D. la Pierre, M. Salvo, M.

- 1 Ferraris, Glass-to-metal seals for solid oxide cells at the Politecnico di Torino, an
2 overview, *Int. J. Appl. Ceram. Technol.* 19 (2022) 1017–1028.
3
4 <https://doi.org/10.1111/ijac.13949>.
5
6
7
8
9 [33] B. Cela Greven, S. Gross-Barsnick, T. Koppitz, R. Conradt, F. Smeacetto, A.
10 Ventrella, M. Ferraris, Torsional shear strength of novel glass-ceramic composite
11 sealants for solid oxide fuel cell stacks, *Int. J. Appl. Ceram. Technol.* 15 (2018)
12 286–295. <https://doi.org/10.1111/ijac.12819>.
13
14
15
16
17
18 [34] L. Wang, W. Yang, Z. Ma, J. Zhu, Y. Li, First-principles study of chromium di ff
19 usion in the ferritic Fe-Cr alloy, *Comput. Mater. Sci.* 181 (2020) 109733.
20
21 <https://doi.org/10.1016/j.commatsci.2020.109733>.
22
23
24
25 [35] A.R. Kampf, R.C. Peterson, B.R. Joy, Itsiite, $\text{Ba}_2\text{Ca}(\text{BSi}_2\text{O}_7)_2$, a new mineral
26 species from Yukon, Canada: Description and crystal structure, *Can. Mineral.* 52
27 (2014) 401–407. <https://doi.org/10.3749/canmin.52.3.401>.
28
29
30
31
32
33
34
35
36
37
38

Figure captions

39 **Figure 1.** Configuration used for the mechanical tensile test.

40
41 **Figure 2.** Heating Stage Microscopy (HSM) curves of the GC2 glass (5°C/min heating rate) on the
42 Fe22Cr porous alloy (curve 1) and on the inert Al_2O_3 support (curve 2); characteristic temperatures
43 of GC2 glass identified with HSM are shown below the figure.
44
45
46

47 **Figure 3.** Dilatometric curves of the GC2 as-cast glass (curve 1) and GC2 glass-ceramic obtained
48 after sinter-crystallization at 950°C for 1h (curve 2); 5°C/min heating rate.
49
50

51 **Figure 4.** SEM images of the cross-section of (a) Crofer22APU/GC2 glass-ceramic/Fe22Cr porous
alloy, (b) Crofer22APU/GC2 glass-ceramic interface (back-scattered) and (c) GC2 glass-
ceramic/Fe22Cr porous alloy interface (back-scattered) obtained after sinter-crystallization at 950°C
for 1h.

1 **Figure 5.** CT-scan of a Crofer22APU/GC2 glass-ceramic/Fe22Cr porous alloy joined sample
2
3 thermally treated at 950°C for 1 h. (a) 3D-model; sectioning plane (b) close to the porous alloy, (c)
4 in the middle of the glass-ceramic, (d) close to Crofer22APU. The big pore on the right could
5 probably be due to the manual slurry method used to produce the joined specimen.
6
7

8
9 **Figure 6.** Cross-section FE-SEM images at lower (a) and higher (b) magnification of the Fe22Cr
10 porous alloy/GC2 glass-ceramic interface after sinter-crystallization at 950°C for 1h; (c) infiltration
11 of the glass-ceramic in the porous alloy of the joined sample; (d) EDS analyses of the GC2 glass-
12 ceramic in the joining area.
13
14
15
16

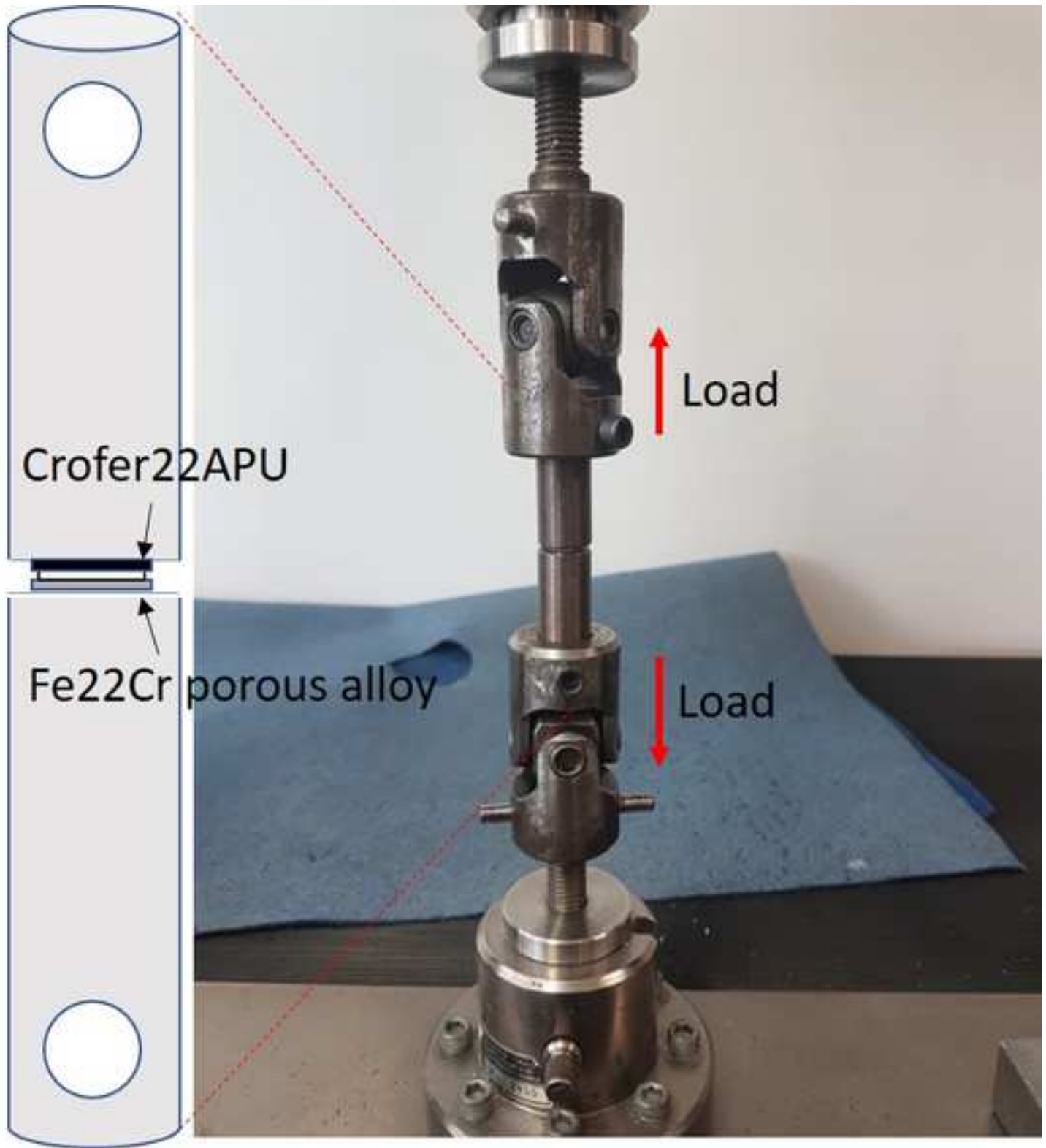
17 **Figure 7.** Macrographs of as-joined and aged Crofer22APU/GC2glass-ceramic/ Fe22Cr samples
18 after tensile testing.
19
20

21 **Figure 8.** SEM images of top views of fracture surface of an as-joined (a) and an aged (b)
22 Crofer22APU/GC2glass-ceramic/ Fe22Cr porous alloy sample after mechanical testing
23 (Crofer22APU side); EDS analyses carried out on the fracture surfaces in the joining area.
24
25
26

27 **Figure 9.** FE-SEM images of a cross-section after ageing at 700°C for 500hrs: (a,c) Fe22Cr porous
28 alloy/GC2 glass-ceramic interface and (b) Fe22Cr porous alloy; (d) higher magnification of Fe22Cr
29 porous alloy and EDS analysis carried out on the porosity edge of the porous alloy.
30
31
32

33 **Figure 10.** XRD pattern of the fracture surface (Crofer22APU side) of a Fe22Cr/GC2 glass-
34 ceramic/Crofer22APU joined sample after ageing at 700°C for 500 hrs.
35
36
37
38





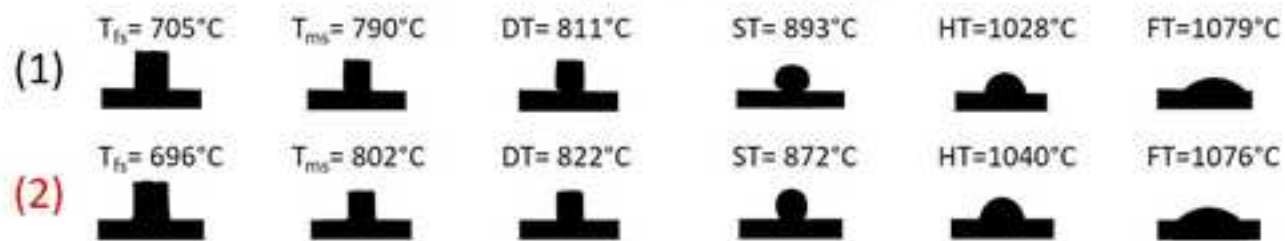
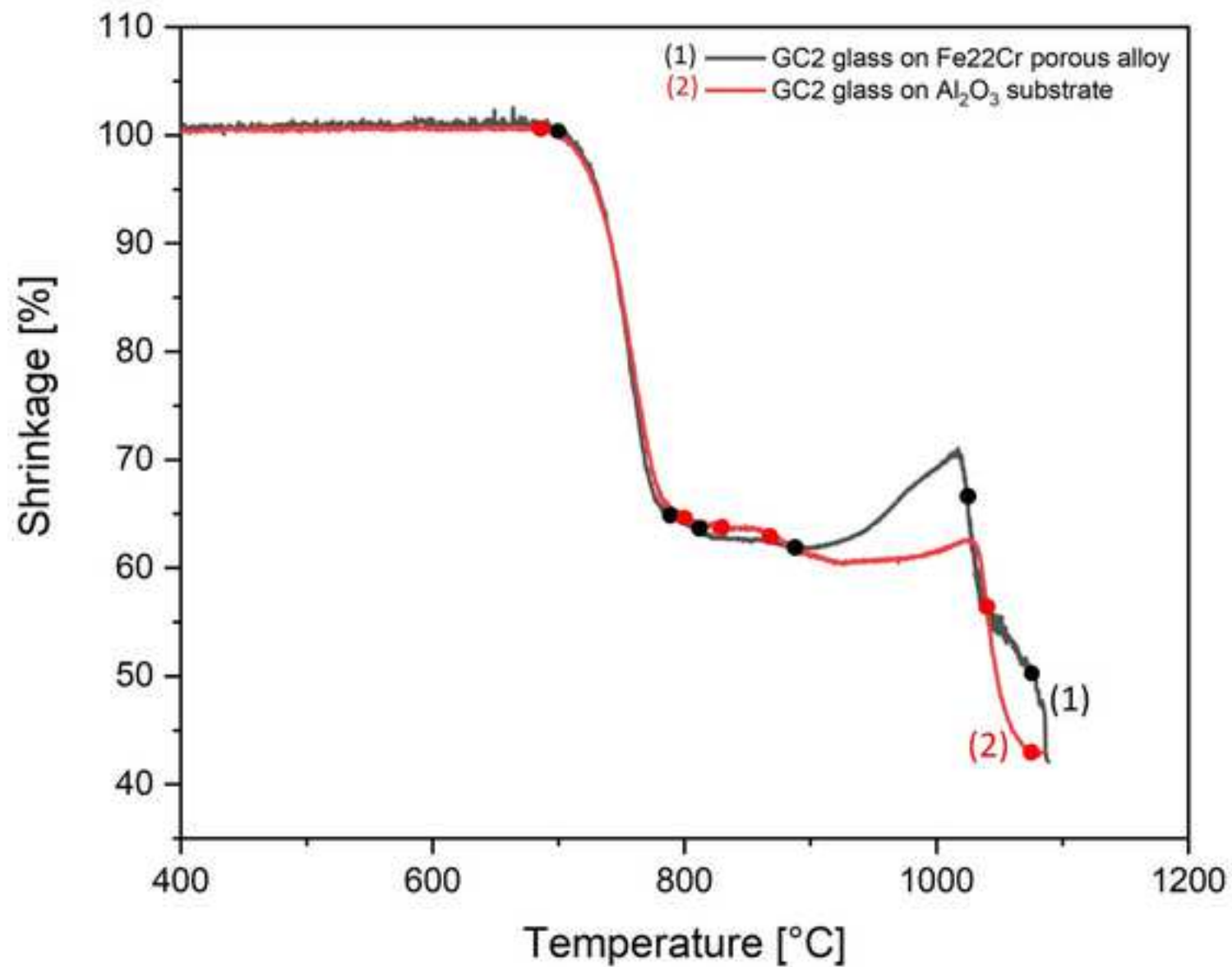
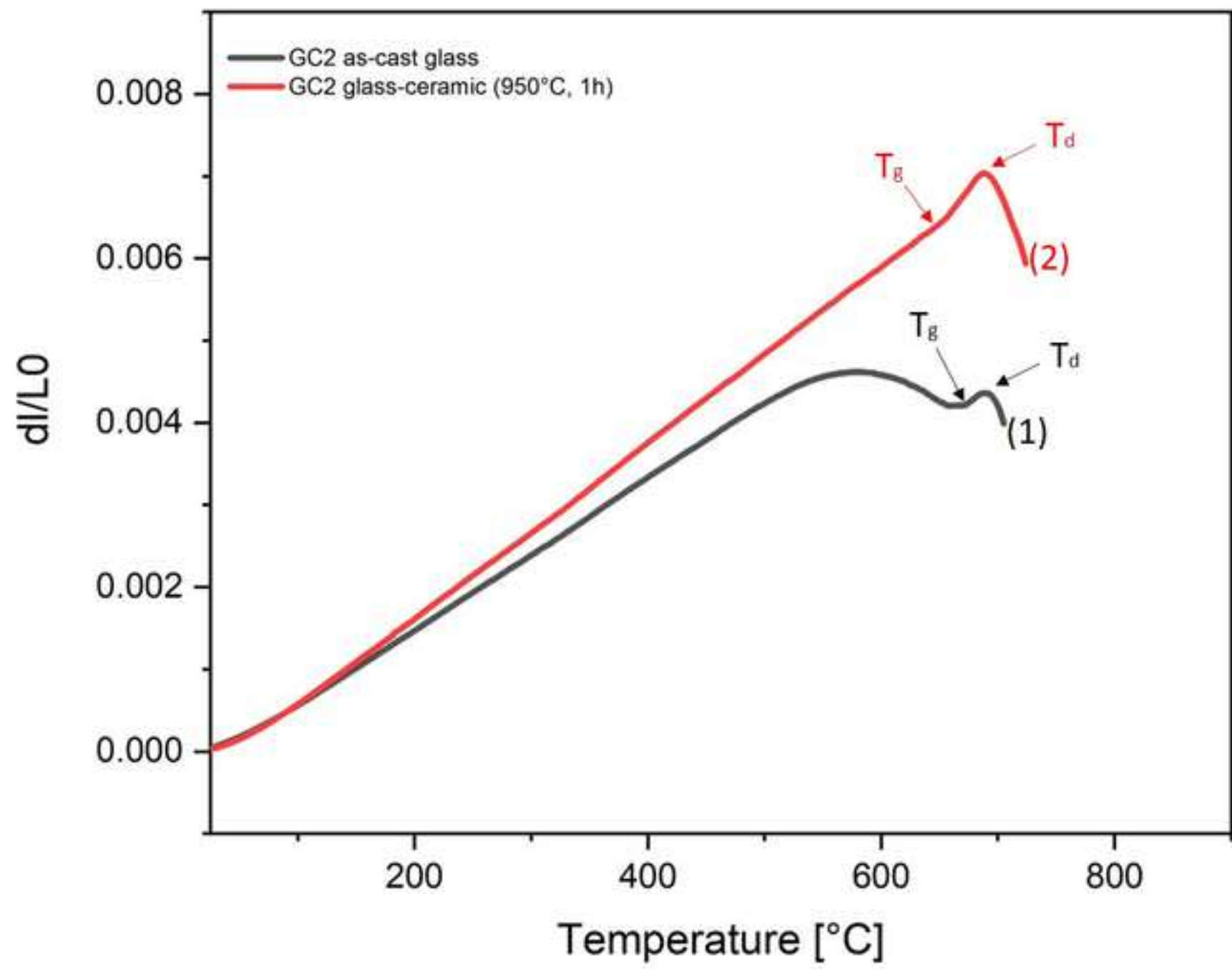
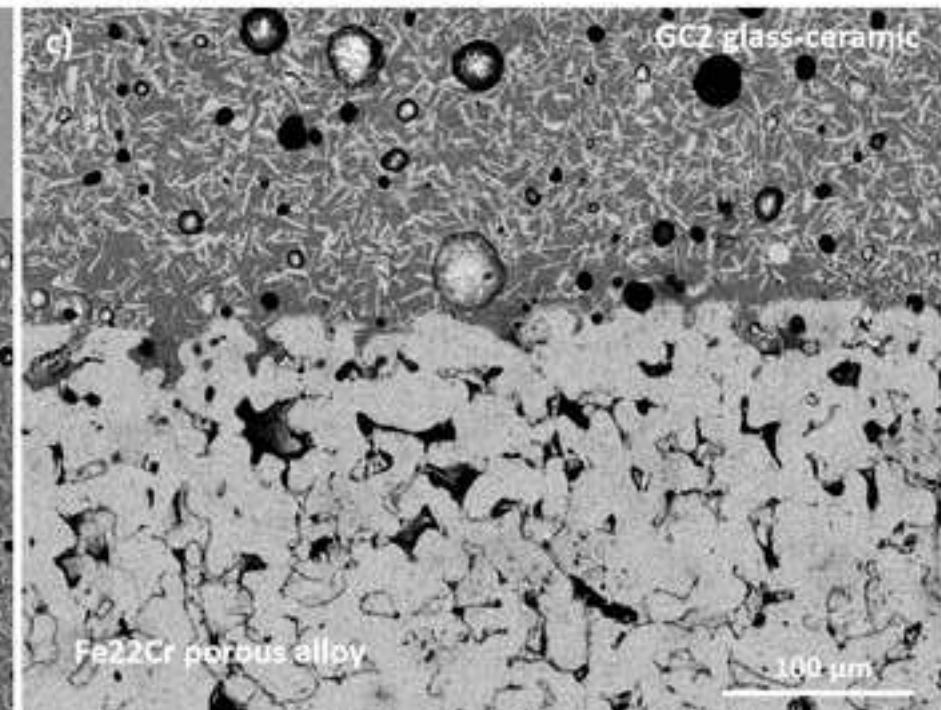
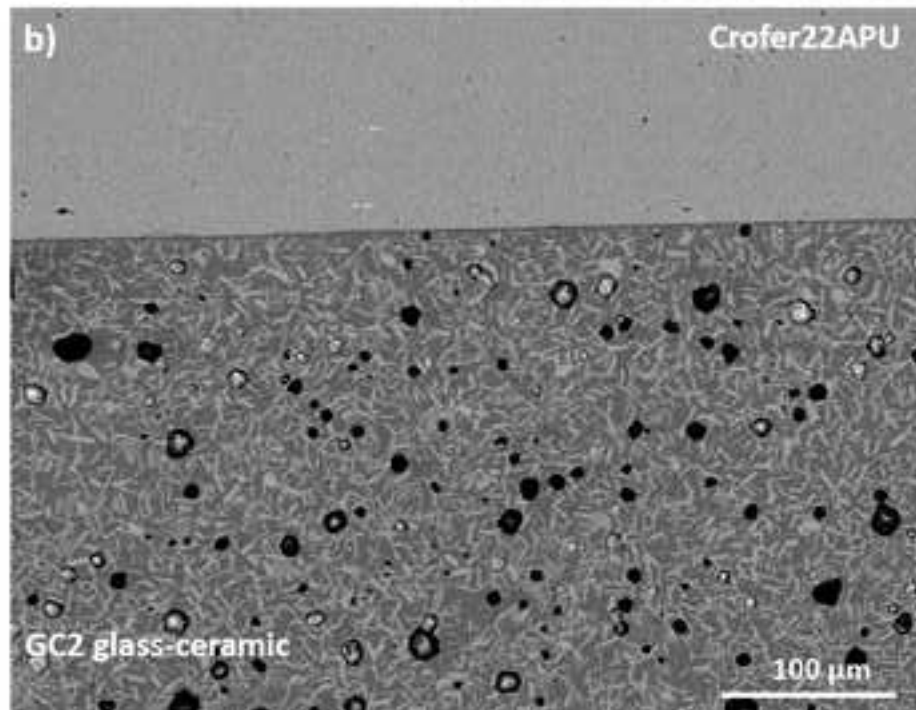
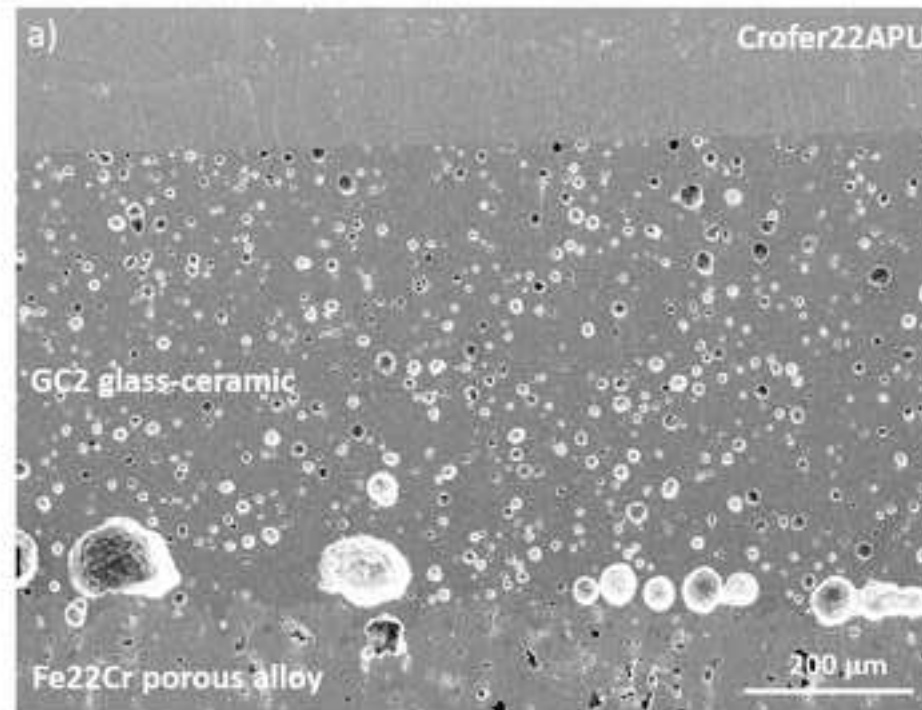
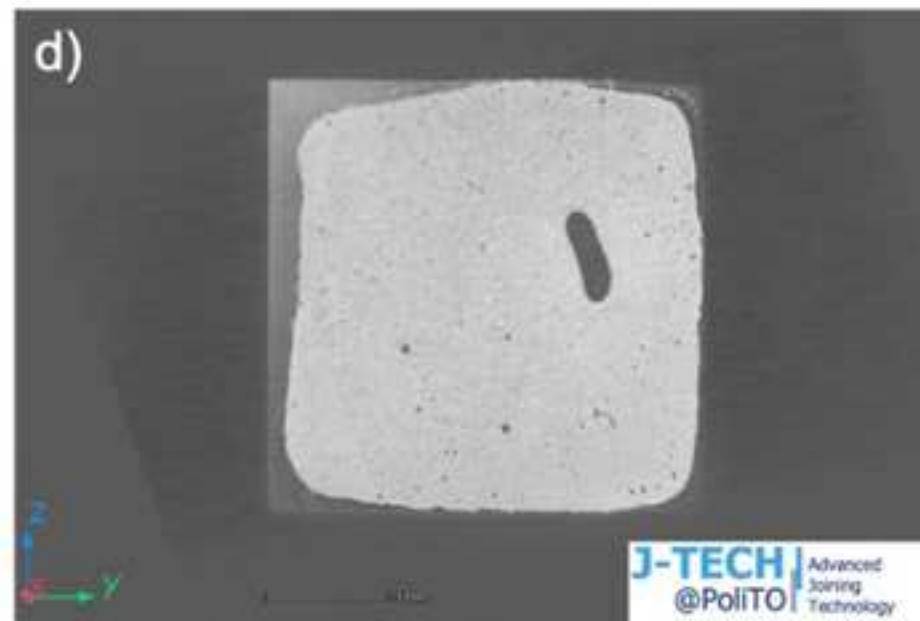
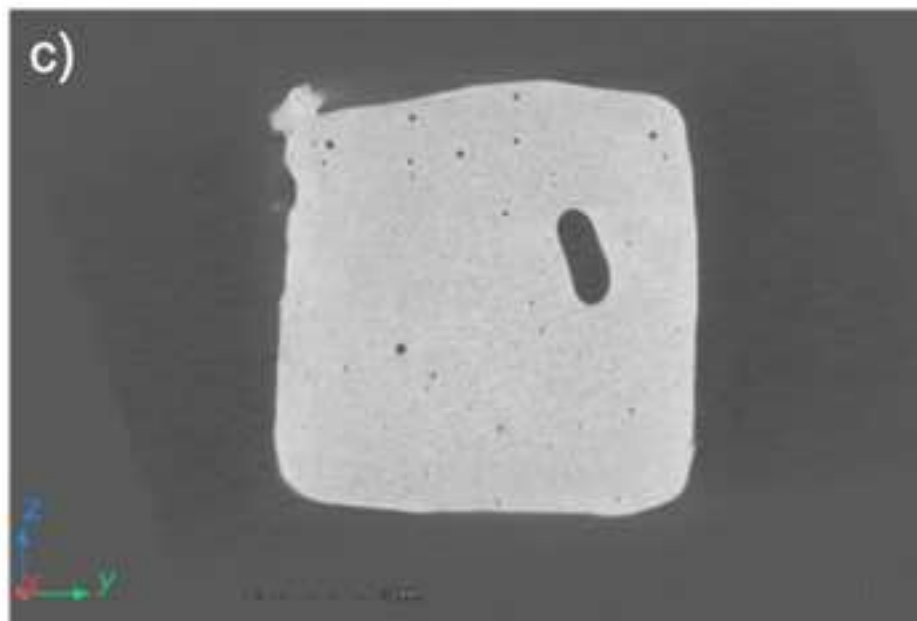
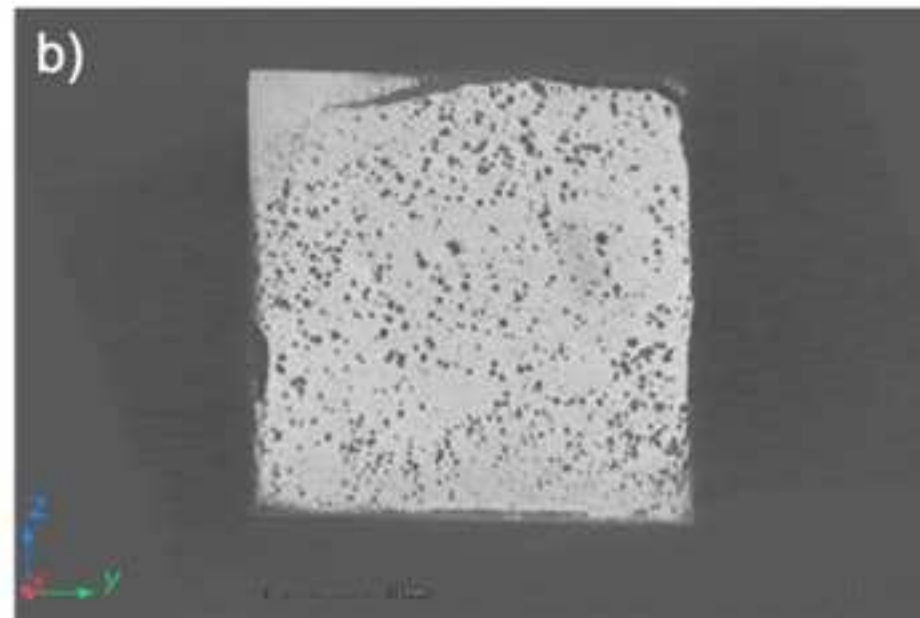
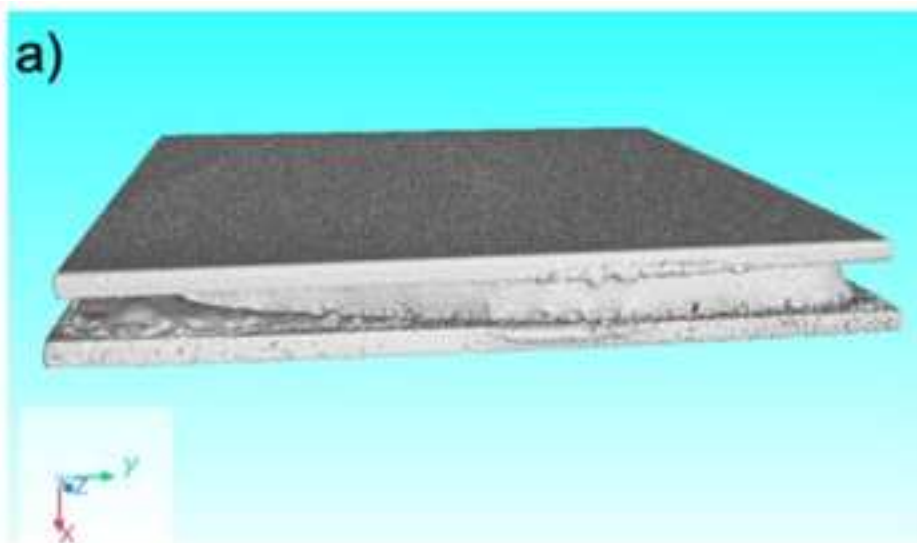
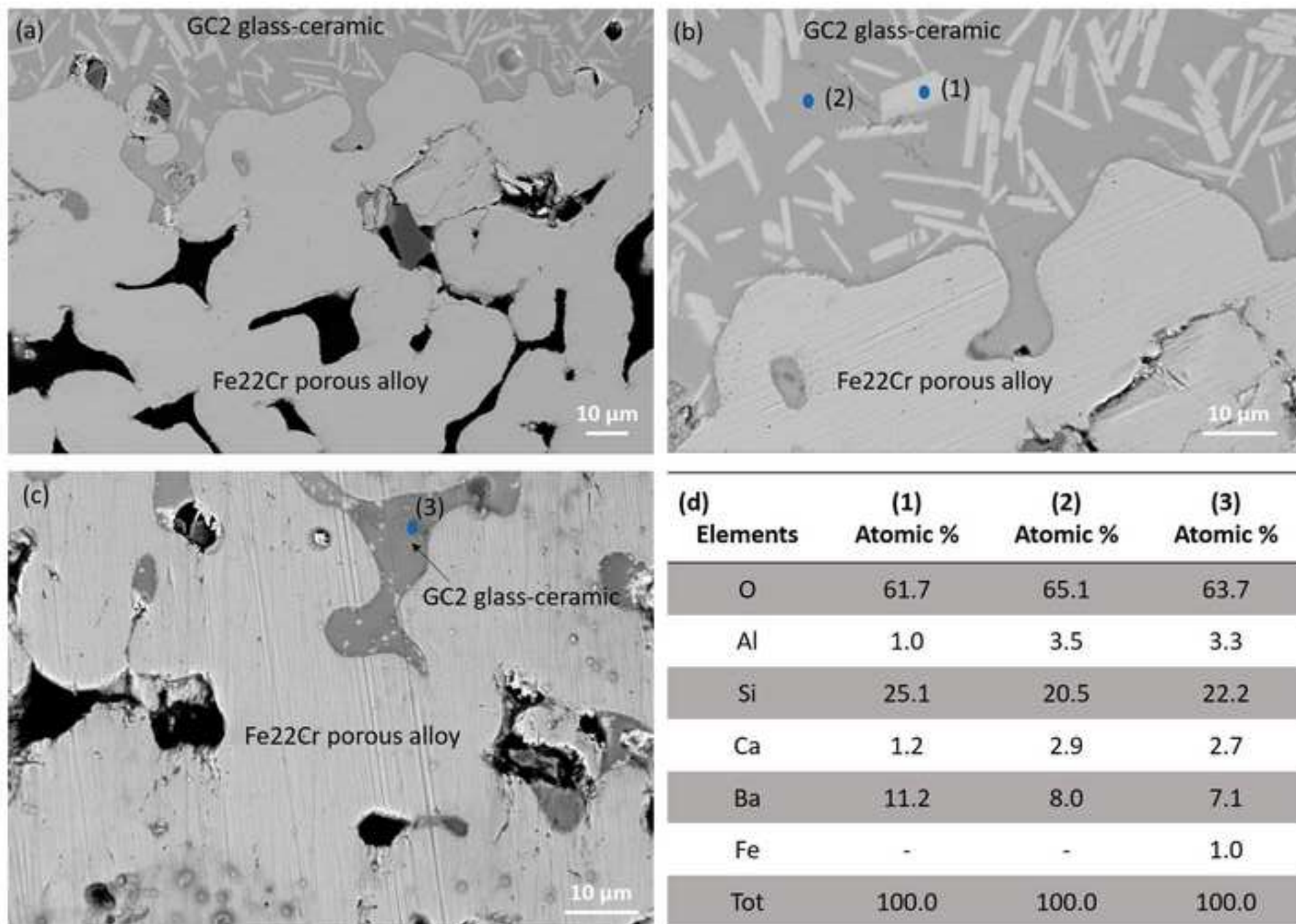





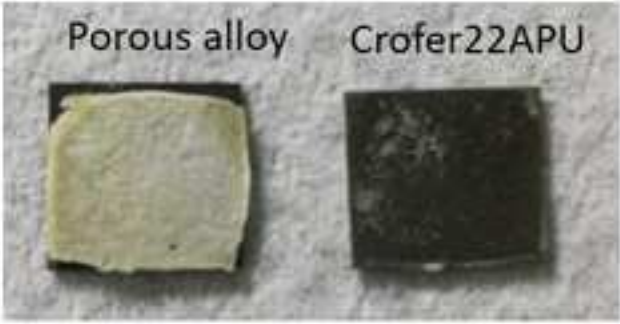
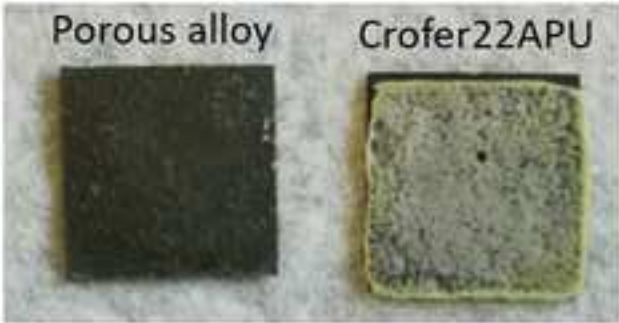

Figure 3









Samples	Before ageing	After ageing
n.1		
n.2		
n.3		
σ_m [MPa]	7.4 ± 0.5	7.7 ± 2.9

